PHYSICAL REVIEW C **108**, 064910 (2023)

3+1D initialization and evolution of the glasma

Scott McDonald,[*] Sangyong Jeon, and Charles Gale
Department of Physics, McGill University, 3600 University Street, Montreal, Quebec, Canada H3A 2T8

(Received 6 July 2023; accepted 17 October 2023; published 21 December 2023)

The IP-GLASMA initial condition has been highly successful in the phenomenology of ultrarelativistic heavy ion collisions. The assumption of boost invariance, however, while good for collision energies probed at the Large Hadron Collider, limits the use of IP-GLASMA to the transverse dynamics of heavy ion collision to near midrapidity. There is a wealth of physics to be explored and understood in the longitudinal dynamics of heavy ion collisions, and a full understanding of heavy ion collisions can only come from three-dimensional studies. In particular, long range rapidity correlations are seeded in the initial collision and provide additional information on the high energy nuclear wave functions that have thus far been inaccessible to the IP-GLASMA model. In this paper, we introduce a way to extend the IP-GLASMA model to 3+1 dimensions while preserving its key features.

DOI: 10.1103/PhysRevC.108.064910

I. INTRODUCTION

Heavy ion collisions (HICs) conducted at the Relativistic Heavy Ion Collider (RHIC) and the Large Hadron Collider (LHC) are sufficiently energetic to create a deconfined state of quarks and gluons known as quark gluon plasma (QGP). Due to their complexity and changing degrees of freedom, no single model is able to describe the entirety of these collisions, and thus they are modeled in stages, usually including independent models for the initial state, a hydrodynamic (QGP) phase, and a hadronic gas phase.

There is broad agreement in the field that nucleus-nucleus collisions create QGP and that this exotic state of matter is governed by relativistic fluid dynamics with an extremely small shear viscosity to entropy density ratio (specific shear viscosity), η/s [1–3]. It is similarly accepted that, as the fluid expands and cools, it hadronizes and can be described by hadron gas dynamics such as those modeled with URQMD [4] or SMASH [5]. The initial state, however, has not reached such a high level of consensus.

Because the outcomes of hydrodynamic simulations are sensitive to the details of the initial conditions, it is important to constrain the initial state before strong statements can be made about details of the QGP phase, such as the transport coefficients. In order to do so, it is important to explore both the transverse and the longitudinal dynamics of HICs. The transverse dynamics has been successfully explored by many via $2+1$-dimensional ($2+1$D) models of the initial condition and the dynamics [6–18].

The focus of this paper is on constructing an IP-GLASMA based $3+1$-dimensional ($3+1$D) initial state model and exploring its physical consequences. In order to do so, it is necessary to have $3+1$D simulations of HICs. This has largely been achieved for the hydrodynamic and hadronic phases of the QGP evolution [19–23]. This paper sets out to generalize the phenomenologically successful IP-GLASMA model [24,25] to $3+1$ dimensions so that the $3+1$D machinery can be fully utilized.

IP-GLASMA provides a $2+1$D initial condition that combines IP-SAT-inspired [26] small-x gluon saturation with classical Yang-Mills (CYM) evolution. It has been extremely successful in describing the transverse dynamics of heavy ion collisions when used to initialize hydrodynamic simulations [27,28]. This includes many different observables across a wide range of collision systems and center of mass energies.

The original IP-GLASMA model assumes boost invariance, which simplifies the geometry of heavy ion collisions to $2+1$ dimensions. This allows for a direct analytic solution of the classical Yang-Mills field and also simplifies numerical evolution of the system. This is a good approximation near midrapidity at high energies such as those explored at the LHC, but remains an approximation nonetheless. Furthermore, asymmetric systems such as p+A collisions cannot be accurately approximated as boost invariant due to their large rapidity dependence. This assumption also limits one to study only the transverse dynamics of heavy ion collisions. By relaxing boost invariance, one gains access to the longitudinal dynamics of heavy ion collisions, where there is a wealth of physics to be explored and understood. In this paper, we relax boost invariance in the IP-GLASMA framework by providing longitudinal structure using the Jalilian-Marian, Iancu, McLerran, Weigert, Leonidov and Kovner (JIMWLK) renormalization group equation [29–35], and solve the CYM equations on a three-dimensional lattice [36–43].

---

[*] Currently at Shift Energy, Inc., 1 Germain Street, Saint John, NB, Canada E2L 4V1.

Published by the American Physical Society under the terms of the Creative Commons Attribution 4.0 International license. Further distribution of this work must maintain attribution to the author(s) and the published article's title, journal citation, and DOI. Funded by SCOAP^3.

The consequences of generalizing the IP-GLASMA to $3+1$ dimensions will be explored through comparison with the boost-invariant case. The $3+1$D initial conditions are evolved hydrodynamically using MUSIC [22,23]. As the system expands and cools, and hadronizes, URQMD is used to simulate resonance decays and hadronic rescatterings. Longitudinal observables are studied and compared to experimental data. One of the consequences we would like to study in this paper is the longitudinal correlations. Correlations and fluctuations present in the high energy nuclear wave functions of the colliding nuclei are imprinted on the system during the initial collision. Some of them will be preserved and detected in the final state and some will not, depending on their nature and strength as well as those of the subsequent evolution of the fireball. It is clear, however, that correlations present at the initial collision constitute the upper bound for long range correlations in rapidity.

There are many reasons why we would like to explore longitudinal dynamics of relativistic heavy ion collisions. One important reason is to see whether our understanding of the QGP dynamics mostly gained from $2+1$D studies will still hold in describing the longitudinal dynamics. For instance, we would like to see whether the values of the viscosities extracted in $3+1$D study are consistent with those extracted in $2+1$D study. We would also like to investigate to what extent the boost-invariant approximation breaks in the plateau region around the midrapidity and what breaks it. It will be also interesting (although we leave it for future study) to see how the asymmetry in the size of the colliding nuclei affects the longitudinal dynamics. Other important topics include the effect of $3+1$D evolution to the longitudinal flux tube and the classical gluon field's influence on the propagation of jet partons inside and outside of the plateau region.

In the following, we first briefly describe the $2+1$D IP-GLASMA initial conditions in Sec. II. Generalization to $3+1$ dimensions is explained in Secs. III–V. The differences between the $2+1$D evolutions and the $3+1$D evolutions are highlighted in Secs. VII and VIII. In Sec. X, the $3+1$D results are compared with ALICE data, and we conclude in Sec. XI.

II. INITIAL CONDITIONS IN 2 + 1 dimensions

The large occupation number of small-x gluons at early times in HICs means that they can be treated, to good approximation, as classical fields. The relevant equations of motion are then the CYM equations:

$$[D_\mu, F^{\mu\nu}] = J^\nu. \tag{1}$$

In this paper, we use the convention $D_\mu = \partial_\mu - igA_\mu$ and the mostly negative metric. Under the assumption that the source particles are moving with the speed of light in the same direction, the source terms, composed of the large momentum fraction (large-x) partons in the individual nuclei, propagate undeflected on the light cone:

$$J^\nu = \delta^{\nu\pm}\rho_{A(B)}(x^\mp, \mathbf{x}) \tag{2}$$

where $x^\pm = (t \pm z)/\sqrt{2}$ are the light-cone coordinates. The upper signs are for the projectile nucleus A moving in the positive z direction and the lower signs are for the target nucleus B moving in the negative z direction. In this limit, it is possible to derive an analytic solution to the initial gauge fields immediately following the collision in terms of the gauge fields of the precollision nuclei A and B.

In light-cone coordinates and Lorentz gauge, the precollision CYM equations reduce to the Poisson equation

$$A^\pm_{A(B)} = -\frac{\rho_{A(B)}}{\nabla_\perp^2 - m^2} \tag{3}$$

where $m = 0.4$ GeV is an infrared regulator that models the color neutrality scale. Here A^+ is for the projectile nucleus and A^- is for the target nucleus. These gauge fields can be gauge transformed to the light-cone gauge by using the following path-ordered Wilson lines:

$$V_{A(B)}(\mathbf{x}_\perp) = P\exp\left(-ig\int dx^\mp \frac{\rho_{A(B)}(x^\mp, x_\perp)}{\nabla_\perp^2 - m^2}\right) \tag{4}$$

the discretized form of which can be written as [44]

$$V_{A(B)}(\mathbf{x}_\perp) = \prod_{i=1}^{N^\mp} \exp\left(-ig\frac{\rho_i^{A(B)}(x_\perp)}{\nabla_\perp^2 - m^2}\right) \tag{5}$$

where $N^\mp$ is typically set to 50. The precollision gauge fields then become purely transverse:

$$A_i = \frac{i}{g} V\partial_i V^\dagger, \tag{6}$$

$$A^\pm = 0. \tag{7}$$

This is the celebrated McLerran-Venugopalan (MV) model [45,46].

These precollision fields can be related to the postcollision gauge fields that reside in the forward light cone by matching the fields on the light-cone boundary, including the source terms. This matching yields the initial glasma fields [47,48] given by

$$A_0^i = A_A^i + A_B^i, \tag{8}$$

$$E_0^\eta = -ig[A_A^i, A_B^i], \tag{9}$$

where again the subscripts A and B refer to the projectile nucleus and the target nucleus, respectively. The coordinate system for the glasma field is the Milne coordinate system where $\tau = \sqrt{t^2 - z^2}$ and $\eta = \tanh^{-1}(z/t)$. The gauge condition for the glasma fields is $A^\tau = 0$. In $2+1$ dimensions, one can identify E^η with $-2A^\eta$ using

$$\begin{aligned} E^\eta &= \frac{1}{\tau}\partial_\tau A_\eta = -\frac{1}{\tau}\partial_\tau(\tau^2 A^\eta) \\ &= -2A^\eta - \tau\partial_\tau A^\eta \end{aligned} \tag{10}$$

where we used the fact that $A_\eta = -\tau^2 A^\eta$ and assumed that the second term vanishes as $\tau \to 0$. For a visual summary of the $2+1$D initial condition, see Fig. 1.

Having determined the initial gauge fields and the longitudinal electric field, it remains to specify the transverse electric field, which must satisfy Gauss's law:

$$\left[D_\eta, E_0^\eta\right] + \left[D_i, E_0^i\right] = 0. \tag{11}$$

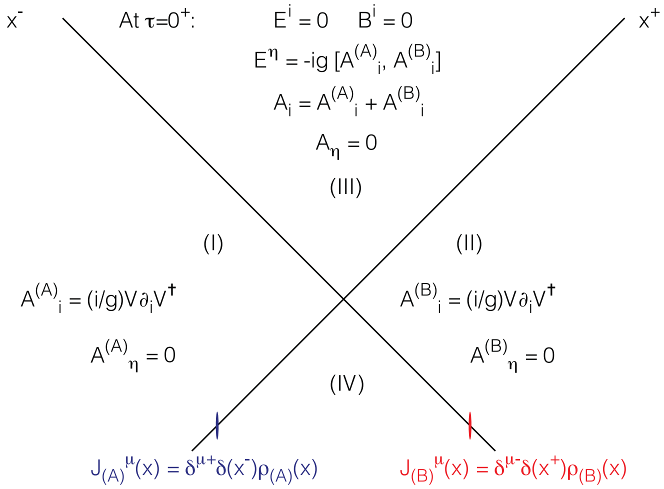

FIG. 1. A summary of the 2 + 1D initial conditions.

The boost invariance of the system make Gauss's law trivial, due to vanishing derivatives in η. The resulting solution is simply $E^i_0 = 0$. This solution is not unique. Any vector field e^i_0 that satisfies $[D_i, e^i_0] = 0$ can be a solution. However, $E^i_0 = 0$ is the most natural choice in view of the fact that the initial transverse chromomagnetic fields $B^i_0 = 0$ because the system is boost invariant and we assumed $A_\eta = 0$ at $\tau = 0^+$.

For nonzero gradients in the rapidity direction, E^i_0 and B^i_0 become nonzero, and their magnitudes are determined by the size of the η gradients. These, in turn, come from the rapidity dependence of the model. In the case of the current paper, the rapidity dependence comes from the JIMWLK renormalization group equation, to be discussed in Sec. V.

III. GENERALIZING TO 3 + 1 dimensions

The beauty of 2 + 1D IP-GLASMA formulation is the availability of the exact solution of the classical Yang-Mill equation Eq. (3) in the infinite momentum (equivalently, in the infinite beam rapidity) limit. Once this condition is relaxed, exact solutions are no longer available. Some possibilities to resolve this issue include the following. One can try to solve the classical Yang-Mills equations numerically provided that the source profile of each nucleus at finite velocity is known. Or one can make an Abelian assumption to solve the 3 + 1D CYM equations analytically as in Refs. [49,50]. One can also try to modify the 2 + 1D solution in such a way to approximate the physical situation. So far, to the authors' best knowledge, most attempts at generalizing the MV model and IP-GLASMA model fall into the last category [43,51–56] and it is also the route we will take. (Other non-IP-GLASMA-related approaches such as flux-tube or string type models also exist [57,58].)

Our general strategy is somewhat similar to the one employed in Ref. [52] but not exactly the same. Consider the usual MV solution of the 2 + 1D Yang-Mills equation Eq. (3) [equivalently, Eq. (6)] given the color charge density $\rho_{A(B)}$. Since the color charge density $\rho_{A(B)}$ does not depend on the rapidity, neither does the gluon field $A^i_{A(B)}$. In other words, in any boosted frame, $A^i_{A(B)}$ looks exactly the same, and hence, the resulting glasma field $A^i = A^i_A + A^i_B$ in any boosted frame looks exactly the same, too. This implies that the produced glasma is boost invariant.

Once we add quantum fluctuations, however, the JIMWLK evolutions of the color densities break the boost invariance by introducing a reference rapidity. In this way, the gluon densities of the projectile and the target nuclei can look *different* in different boosted frames, equivalently at different space-time rapidity $\eta = \tanh^{-1}(t/z)$. Consider a world line passing through the origin of the center of mass frame so that $z/t = v_z$ is a constant. This also represents a world line where the space-time rapidity η is constant. One can therefore get the initial condition at η by considering how the projectile and the target nuclei appear in the frame boosted by $v_z = \tanh\eta$. This is illustrated in Fig. 2.

In Ref. [52], this idea was used to get the initial condition for the 3 + 1D evolution of the glasma field. The difference here is in the way the longitudinal dynamics is treated. In Ref. [52], each transverse plane at different η evolves independently of each other following the usual 2 + 1D IP-GLASMA formulation of the initial condition and evolution. On the other hand, we keep the longitudinal interaction between the transverse planes at different rapidities. To do so, however, complicates not only the evolution of the system but also the initial condition.

IV. INITIAL A_η AND E_i

There has been significant effort in recent years on 3 + 1D classical Yang-Mills in the context of heavy ion collisions. Each of these efforts has implemented some type of rapidity dependence, whether it be through rapidity fluctuations [36,37,59], JIMWLK evolution [52], or color sources [43,53,54]. In this paper, we extend the initial conditions themselves to be able to accommodate a non-boost-invariant setup.

One of the consequences of having an η dependence is that the usual 2 + 1D solution, $A_i = (i/g)V\partial_i V^\dagger, A_\eta = 0$, is no longer pure gauge in space. This introduces a problem in energy deposition because the field strength $F_{\eta i}$ no longer vanishes outside the overlap region. This chromomagnetic field component automatically vanishes in the 2 + 1D case outside the overlap. However, in three dimensions, the derivative in η no longer vanishes and hence if one were to use the 2 + 1D MV solution for individual nuclei one would find $F_{\eta i} = \partial_\eta A_i \neq 0$. This means that nonzero energy density would appear in the transverse plane wherever a single nucleus had nonzero gauge field, rather than solely in the interaction region. This phenomenon can be seen clearly in Fig. 3.

This undesirable feature can conceivably be dealt with in two ways. One is to just remove the energy density from the positions where either A^i_A or A^i_B vanishes. This option, however, is ambiguous since it is not clear whether any subtraction should be made in the regions where neither of the two fields vanishes. Another more natural option is to generalize the initial condition by modifying the longitudinal gluon

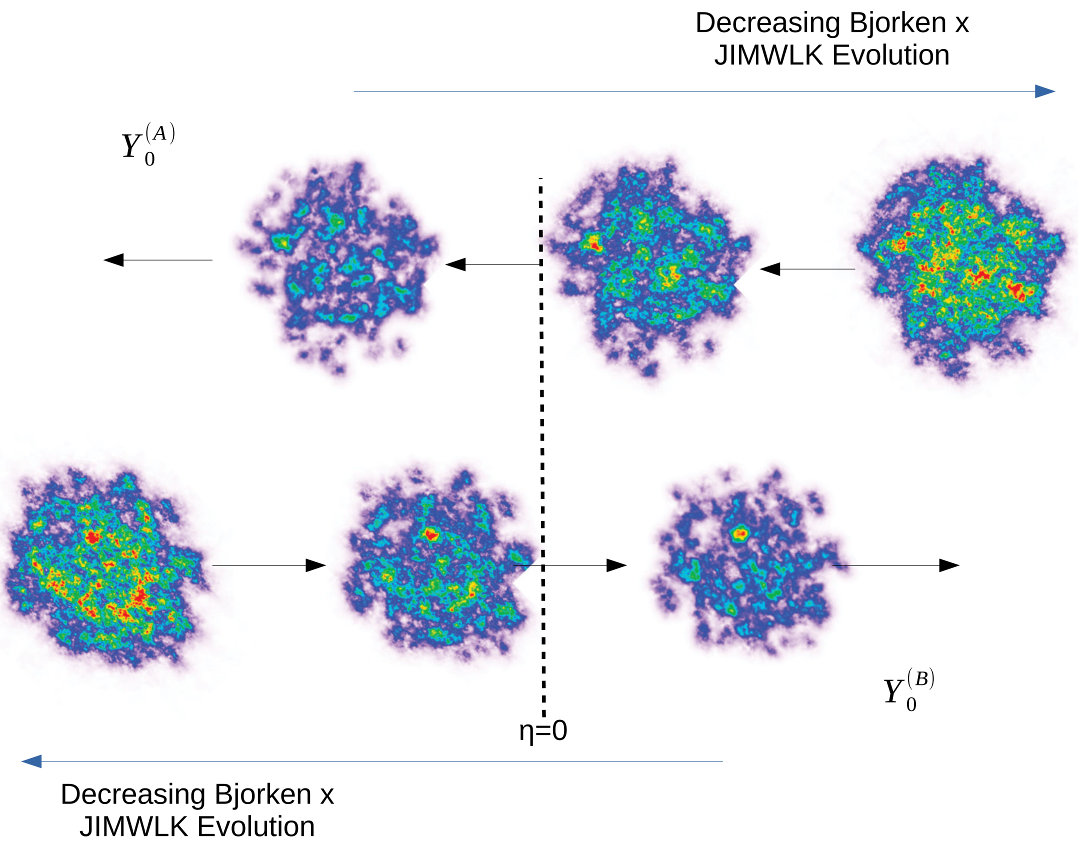

FIG. 2. Two nuclei evolving in rapidity via the JIMWLK equations. At $Y_A^{(0)}$ and $Y_B^{(0)}$ the Wilson lines are determined via Eq. (5). Then these Wilson Lines are evolved via Eq. (18). Plotted are snapshots of the quantity $\frac{1}{N_c}\mathrm{Tr}(V-1)$, a proxy for gluon density. It is possible to see as the JIMWLK evolution proceeds to smaller Bjorken x that the gluon density increases while the large scale geometry of the nuclear structure persists.

fields as

$$A_{0,\eta}^{A\,(B)} = \frac{i}{g} V_{A\,(B)} \partial_\eta V_{A\,(B)}^\dagger, \tag{12}$$

$$A_{0,\eta} = A_\eta^A + A_\eta^B \tag{13}$$

which are calculated just above the light-cone axes inside the forward light cone. This has the advantage of retaining the feature that each individual nucleus remains pure gauge in space, while reducing to the boost-invariant case where derivatives in η vanish. Recall that the field strength tensor of a pure gauge vanishes, and thus does not contribute to the energy density. For a visual summary of the $3+1$D initial condition, see Fig. 4.

It is worth noting here that, in general, initial conditions are needed for the dynamic variable A_η and its conjugate momentum E^η but not A^η. The fact that we could specify the initial value for A^η as $-E_0^\eta/2$ in $2+1$ dimensions is due to the fact that we need to require $A_\eta \to 0$ in the $\tau \to 0$ limit to prevent the transverse energy density from diverging in the same limit. Such a requirement forces the behavior of A_η in the small τ limit to be $A_\eta = (E_0^\eta/2)\tau^2 + O(\tau^3)$. However, this is not the only possibility. One can have

$$A_\eta(\tau) = A_{0,\eta} + \frac{E_0^\eta}{2}\tau^2 + O(\tau^3) \tag{14}$$

and still get

$$E^\eta = \frac{1}{\tau}\partial_\tau A_\eta = E_0^\eta + O(\tau) \tag{15}$$

in the small τ limit as long as both $A_{0,\eta}$ and E_0^η depend only on $\mathbf{x}_\perp$ and η and not on τ. Hence, in the absence of any additional conditions, $A_{0,\eta}$ is arbitrary. In $2+1$ dimensions, we need to choose $A_{0,\eta} = 0$ to keep the transverse energy density from diverging at the initial time $\tau_0 = 0^+$. In $3+1$ dimensions, $\tau_0 \neq 0$ and hence we can exploit this freedom to consistently remove unwanted energy deposits.

Another consequence of having the η dependence is that the solution to Gauss's law is now nontrivial. In fact, Gauss's law is underconstrained, as it provides only one equation for two unknown fields, E^x and E^y. It is possible to find a solution by relating the two unknown fields through the following ansatz:

$$E_0^i = [D^i, \phi_0]. \tag{16}$$

This ansatz turns Gauss's law into the covariant Poisson equation

$$[D_i, [D^i, \phi_0]] = -\big[D_\eta, E_0^\eta\big] \tag{17}$$

which can be solved iteratively through a modified Jacobi method (see Appendix A for numerical details). This ansatz leads to a solution to Gauss's law in the non-boost-invariant

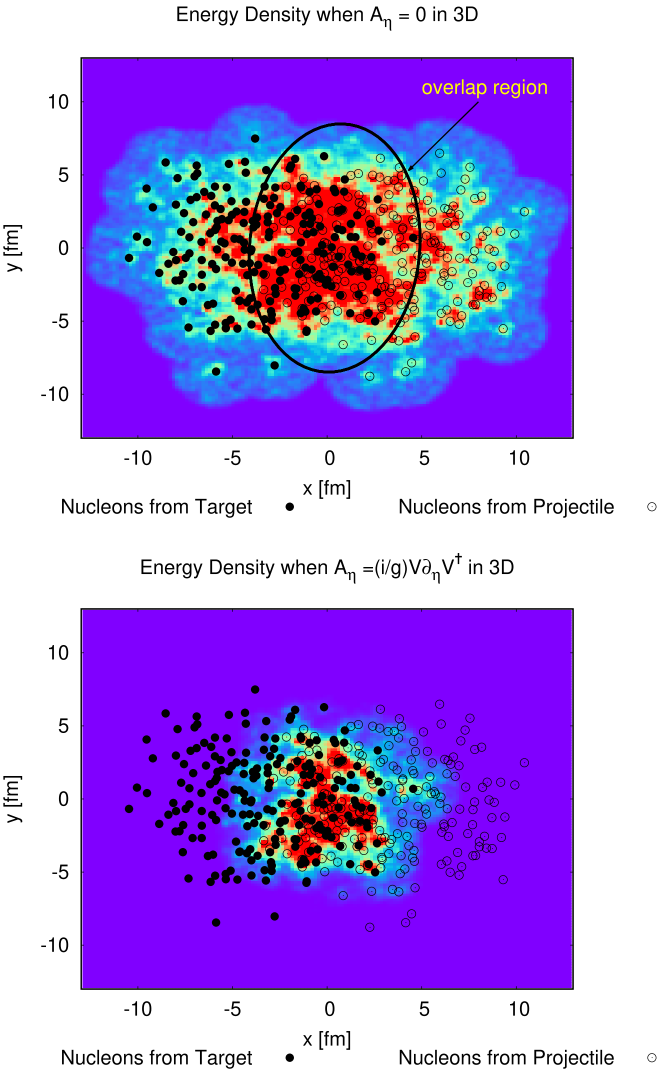

FIG. 3. The upper figure demonstrates the problem of initializing $A_\eta = 0$ on a three-dimensional lattice, namely that there is nonzero energy density outside of the overlap region of the two nuclei. The lower panel, in contrast, shows that initializing according to Eq. (3) eliminates this problem.

system. This solution is, however, not unique. One can always add another vector field e_0^i that is nondivergent in two dimensions ($[D_i, e_0^i] = 0$) and still satisfy the Gauss law. In this paper, we simply set $e_0^i = 0$, which is consistent with the conditions that the initial glasma field should vanish outside the interaction region and that the total energy deposit should have a reasonable value for RHIC and the LHC heavy ion collisions. In our simulations, the lattice equation of motion preserves the lattice Gauss law.

V. JIMWLK EVOLUTION

The color glass condensate is predicated on the idea that the gluon density of high energy nuclei will begin to saturate as the gluon density becomes sufficiently high for gluon recombination to compete with gluon radiation. It relies on a separation of scales, in which the large momentum fraction, or large-x, partons serve as sources for the small-x gluons.

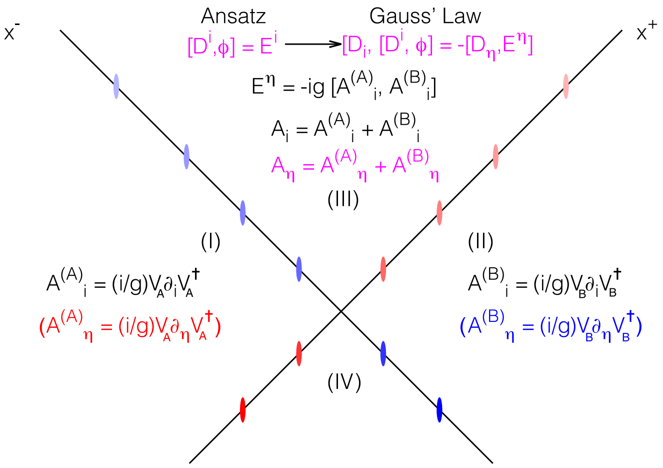

FIG. 4. A summary of the 3 + 1D initial conditions. The parentheses around $A_\eta^{(A)}$ and $A_\eta^{(B)}$ indicate that these fields do not reside in regions I and II but are calculated just inside region III.

The JIMWLK [30,31] renormalization group equation integrates out the quantum fluctuations around the classical background field and changes the effective source term for the small-x gluons. In this way, the JIMWLK evolution introduces a rapidity dependent charge per unit area, while preserving the form of the gluon Lagrangian. The JIMWLK evolution gives the model its rapidity dependence through the stochastic gluon radiation that follows from the rapidity evolution.

The form of the JIMWLK equation used in this paper is from Ref. [35] and given in terms of the Langevin step:

$$V_{A(B)}(\mathbf{x}, Y + dY) = \exp\left(-i\frac{\sqrt{dY}}{\pi}\int_{\mathbf{u}}\mathbf{K}_{\mathbf{x}-\mathbf{u}}\cdot\left(V_u\boldsymbol{\zeta}_u V_u^\dagger\right)\right) \times V_{A(B)}(\mathbf{x}, Y)\exp\left(i\frac{\sqrt{dY}}{\pi}\int_{\mathbf{v}}\mathbf{K}_{\mathbf{x}-\mathbf{v}}\cdot\boldsymbol{\zeta}_v\right) \tag{18}$$

where $\boldsymbol{\zeta}_z = \{\zeta_1^a(\mathbf{z}, Y)t^a, \zeta_2^a(\mathbf{z}, Y)t^a\}$ is a random variable and $V_u = V_{A,B}(\mathbf{u}, Y)$. Here Y can be either the dynamic rapidity or the space-time rapidity. The correlator for $\boldsymbol{\zeta}$ in this case is given by

$$\langle\zeta^{a,i}(\mathbf{x}, Y_1)\zeta^{b,j}(\mathbf{y}, Y_2)\rangle = \delta^{ab}\delta^{ij}\delta^{Y_1Y_2}\int\frac{d^2\mathbf{k}}{(2\pi)^2}e^{i\mathbf{k}\cdot(\mathbf{x}-\mathbf{y})}\alpha_s(\mathbf{k}) \tag{19}$$

where the noise correlator has a Kronecker delta for (Y_1, Y_2), rather than a delta function, because the $1/dY$ has already been incorporated into Eq. (18). The modified kernel, as used in Ref. [60], is given by

$$\mathbf{K}_{\mathbf{x}-\mathbf{z}} = m|\mathbf{x}-\mathbf{z}|K_1(m|\mathbf{x}-\mathbf{z}|)\frac{(\mathbf{x}-\mathbf{z})}{|\mathbf{x}-\mathbf{z}|^2} \tag{20}$$

where $K_1(x)$ is the Bessel function of the second kind.

The expression in the exponent of Eq. (18) is computed by Fourier transforming the kernel and the noise terms, thus

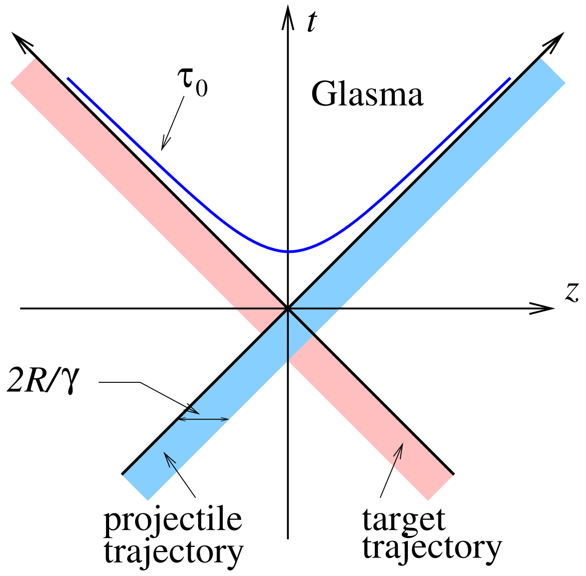

FIG. 5. Positioning of the t and z axes.

turning the two-dimensional integration into a convolution [61]. This improves numerical speed considerably. The Fourier transform of the kernel is given by

$$\mathbf{K}_{\mathbf{k}} = \frac{2\pi i\mathbf{k}}{k^2+m^2}. \tag{21}$$

The form of the running coupling is taken to be

$$\alpha_s(\mathbf{k}) = \frac{4\pi}{\beta \ln\left[\left(\frac{\mu_0^2}{\Lambda_{\rm QCD}^2}\right)^{1/c} + \left(\frac{\mathbf{k}^2}{\Lambda_{\rm QCD}^2}\right)^{1/c}\right]^c} \tag{22}$$

with $\beta = 11 - 2N_f/3$, $\Lambda_{\rm QCD} = 0.2$ GeV, $c = 0.2$, and $\mu_0 = 0.4$ GeV following the prescription in Ref. [35].

In principle, the scale at which the noise fluctuations occur should not exceed the saturation scale, as it is the only physical scale in the problem. However, the noise correlator is a three-dimensional delta function, which means the numerical fluctuations take place at the scale of the inverse lattice spacing $\approx 1/a$. Incorporating the running coupling in the kernel acts to filter out higher $|\mathbf{k}|$ modes. Physically, this means that the scale of the running coupling is taken to be that of the emitted gluon.

VI. EQUATIONS OF MOTION

The evolution of glasma in this paper is performed in the τ-η coordinate system. As in 2 + 1 dimensions, the source terms in the Lagrangian are assumed to be eikonal and propagate along the light-cone axes. Furthermore we set up our coordinate system in such a way that the source currents are below the light-cone axes as shown in Fig. 5. In this way, even though the sources have a finite thickness, the forward light cone is source free and the equation of motion is simply

$$[D_\mu, F^{\mu\nu}] = 0 \tag{23}$$

for $\tau > 0$. Had we set up our coordinate system so that the leading edges of the nuclei define $x^\pm$ instead of the trailing edges, the forward light cone would not be source free. Had we used the Minkowski coordinate system, there would also be regions in z that are not source free [43,53].

The degrees of freedom that are evolved explicitly in time are the electric field and the gauge links in the temporal gauge ($A^\tau = 0$). Starting from the Hamiltonian

$$H = \tau \int d\eta \int d^2x_\perp(\epsilon_\eta + \epsilon_x + \epsilon_y) \tag{24}$$

where

$$\epsilon_{i=x,y} = \frac{1}{2}\frac{1}{\tau^2}[(E^i)^2 + (B^i)^2], \tag{25}$$

$$\epsilon_\eta = \frac{1}{2}[(E^\eta)^2 + (B^\eta)^2] \tag{26}$$

are the transverse and longitudinal energy densities, the Hamiltonian equations of motion for the gauge fields can be derived as

$$\tau\partial_\tau A_i = E^i, \tag{27}$$

$$\frac{1}{\tau}\partial_\tau A_\eta = E^\eta \tag{28}$$

and

$$\partial_\tau E^i = \frac{1}{\tau}[D_\eta, F_{\eta i}] + \tau[D_j, F_{ji}], \tag{29}$$

$$\partial_\tau E^\eta = \frac{1}{\tau}[D_j, F_{j\eta}]. \tag{30}$$

The lattice version of these equations and the numerical method we use to solve them closely follow those in Ref. [37].

Because of $1/\tau$ factors in the equations, the initial time cannot really be pushed to $\tau = 0$. At LHC energies, the saturation scale used in this paper is $Q_s \approx 2$–5 GeV, which corresponds to $1/Q_s \approx 0.04$–0.2 fm. In Ref. [37], it was argued that the initial proper time τ_0 should be much smaller than $1/Q_s$. In this paper, the initial time is set to $\tau_0 = 0.01$ fm.

To deal with the $1/\tau$ factors in the equations, early time evolutions require very small time steps so that $\Delta\tau/\tau \ll 1$. For this reason, variable time steps are employed in the following form:

$$\Delta\tau = \Delta\xi \tanh\frac{\tau}{T_0} \tag{31}$$

or $\xi = T_0 \ln[\sinh(\tau/T_0)]$. This form interpolates between two limiting behaviors. For $\tau \ll T_0$, the time step behaves like $\Delta\tau \approx \Delta\xi(\frac{\tau}{T_0})$ while for $\tau > T_0$ it behaves like $\Delta\tau \approx \Delta\xi$ with $\Delta\xi$ fixed. This achieves the goal of producing small time steps for small τ and larger equal time steps for later times when the $1/\tau$ factors are no longer very large. In this paper, T_0 is set to 0.2 fm and $\Delta\xi$ is set to $\tau_0/2 = 0.005$ fm.

VII. FIELDS AND PRESSURE

As already discussed, the initial transverse chromoelectric and chromomagnetic fields vanish in the boost-invariant case. In 3 + 1 dimensions, this is no longer the case and the transverse fields actually dominate the energy density at early times due to the factor of $1/\tau^2$ in their contribution to the energy density.

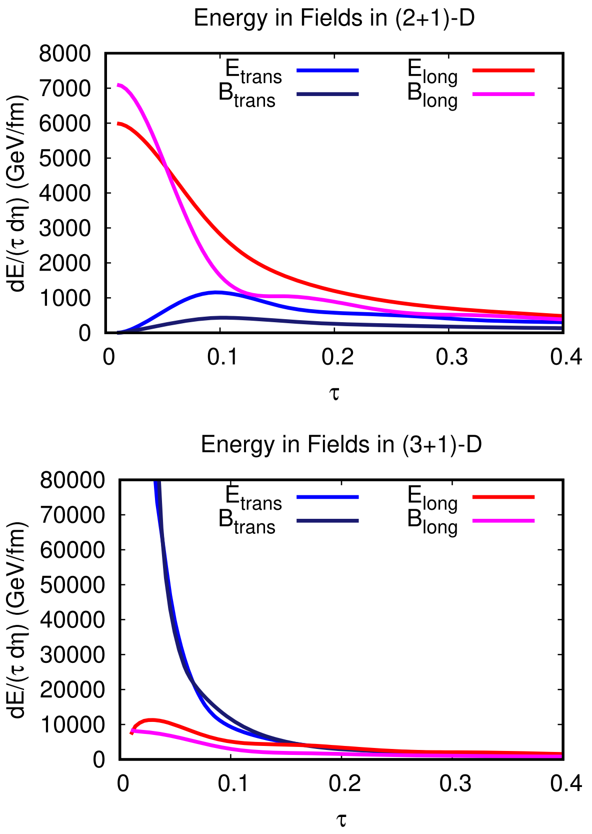

FIG. 6. Left: The time evolution, in fm, of the energy density in the different field components in $2+1$ dimensions. Right: The same quantity as the left panel plotted for the $3+1$D implementation. Both results are computed using the same $3+1$D software, but with the initial $2+1$D and $3+1$D setups, respectively.

The evolution of the energy density in the fields can be seen for both the $2+1$D and $3+1$D scenarios in Fig. 6 where we plot

$$\frac{1}{\tau}\frac{dE(\tau)}{d\eta} = \int d^2x_\perp(\epsilon_\eta + \epsilon_x + \epsilon_y). \tag{32}$$

It is clear that the early time behavior is quite different: In $2+1$ dimensions, the transverse fields vanish at $\tau = 0$ and grow steadily until their contribution to the energy density is comparable to the longitudinal fields. Similar behaviors were also observed in Ref. [24]. In contrast, in $3+1$ dimensions, the transverse fields provide the dominant contribution to the energy density initially. By typical hydrodynamic initialization times of $\tau = 0.2$–0.6 fm, the $3+1$D fields all have similar contributions to the energy, as is the case in $2+1$ dimensions.

The early time behavior of the fields in $3+1$ dimensions causes the longitudinal and transverse pressures to behave quite differently than in the boost invariant case (similar behavior was observed in Ref. [43]). To see why, it is convenient to first express the diagonal components of the stress energy tensor in terms of the quantities defined in Eqs. (25) and (26):

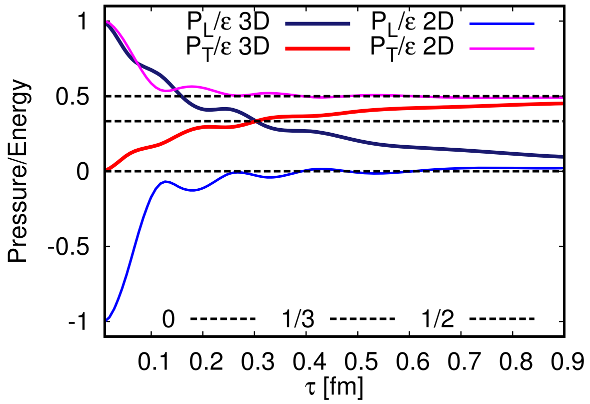

FIG. 7. Comparison of the transverse and longitudinal pressures in the $2+1$D and $3+1$D IP-GLASMA formulations. Both results are computed using the same $3+1$D software, but with the initial $2+1$D and $3+1$D setups, respectively.

$$\begin{aligned} T^{\tau\tau} &= \epsilon_x + \epsilon_y + \epsilon_\eta = \epsilon, \\ T^{ii} &= -\epsilon_i + \epsilon_j + \epsilon_\eta \Big|_{\substack{i=x,y\\ j\neq i}}, \\ \tau^2 T^{\eta\eta} &= \epsilon_x + \epsilon_y - \epsilon_\eta \end{aligned} \tag{33}$$

where T^{ii} is either T^{xx} or T^{yy}. The pressure to energy ratios are given by

$$\frac{P_L}{\epsilon} = \frac{\tau^2 T^{\eta\eta}}{T^{\tau\tau}}, \quad \frac{P_T}{\epsilon} = \frac{T^{xx} + T^{yy}}{2T^{\tau\tau}}. \tag{34}$$

As can be seen in Fig. 7, the $\tau \to 0^+$ limit is quite different in $2+1$ and $3+1$ dimensions:

$$\lim_{\tau\to 0^+} \frac{P_L}{\epsilon} = \begin{cases} \frac{\epsilon_x+\epsilon_y}{\epsilon_x+\epsilon_y} = 1 & \text{in 3+1 dimensions} \\ \frac{-\epsilon_\eta}{\epsilon_\eta} = -1 & \text{in 2+1 dimensions} \end{cases}. \tag{35}$$

and

$$\lim_{\tau\to 0^+} \frac{P_T}{\epsilon} = \begin{cases} \frac{\epsilon_\eta}{\epsilon_x+\epsilon_y} = 0 & \text{in 3+1 dimensions} \\ \frac{\epsilon_\eta}{\epsilon_\eta} = 1 & \text{in 2+1 dimensions.} \end{cases} \tag{36}$$

This is because $\epsilon_{x,y}/\epsilon_\eta \approx 1/\tau^2$ in the small τ limit in $3+1$ dimensions while $\epsilon_{x,y} = 0$ at $\tau = 0^+$ in $2+1$ dimensions. Because of the tracelessness of $T^{\mu\nu}$, the intersection of the pressures necessarily occurs at $\epsilon/3$ in $3+1$D evolution, the condition for pressure isotropy. The pressure does not remain isotropic, however, and approaches the $2+1$D asymptotic behavior for large τ, as the longitudinal pressure freestreams towards zero in both cases. At around the typical hydrodynamic switching time ($\tau \approx 0.4$), the deviation from the pressure isotropy is 10–20%. Viscous MUSIC currently allows for applications with such anisotropic initial conditions. It will be, however, interesting to see how incorporating an additional kinetic theory stage such as the Kømpøst [62,63] or employing AHYDRO [64,65] would compare with our current results. Further studies will form the basis of future investigations.

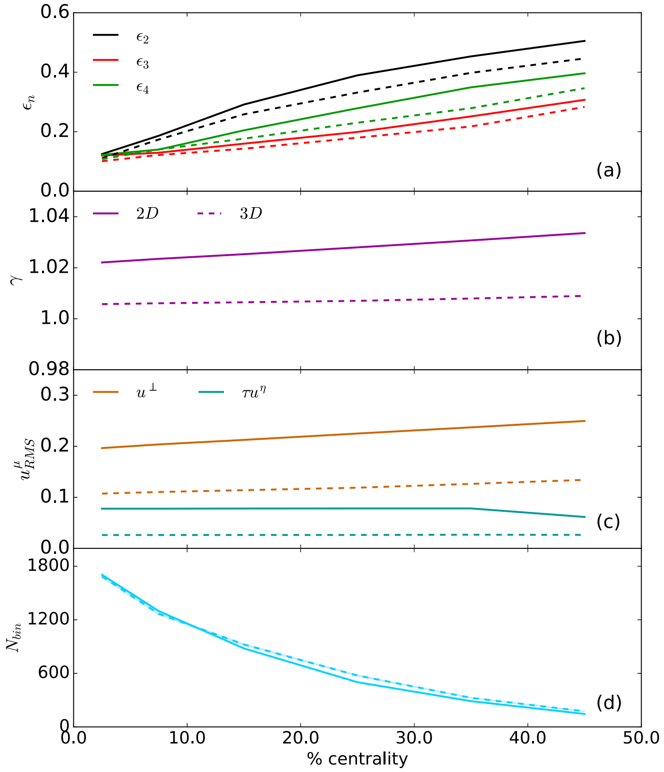

FIG. 8. A comparison between the 3 + 1D IP-GLASMA presented in this paper and the 2 + 1D IP-GLASMA in Ref. [28]. Panel (a) compares the eccentricities between the two simulations. In panel (b), $\gamma = u^\tau$ is plotted, and panel (c) shows the longitudinal and transverse components of the flow velocity. Finally, panel (d) compares the number of binary collisions, $N_{\rm bin}$, as a way of gauging how the two different centrality selection procedures compare. The 3 + 1D curves are calculated at $\tau = 0.6$ fm and the 2 + 1D curves are calculated at $\tau = 0.4$ fm, which are the respective hydrodynamic switching times.

Comparing the 2 + 1D and 3 + 1D pressure curves, P_T/ϵ is substantially larger in 2 + 1 dimensions for the entire evolution up to the typical hydrodynamic switching time that is used, $\tau = 0.4$ fm. This can be seen clearly in Fig. 7. More transverse pressure should mean more transverse flow, and indeed that is what is seen in Fig. 8(c), which compares the transverse and longitudinal flow between the two simulations. One can readily see that the transverse flow develops more rapidly in the 2 + 1D simulations. It needs to be noted that the 3 + 1D curves in Fig. 8 correspond to $\tau = 0.6$ fm, whereas the 2 + 1D curves are at $\tau = 0.4$ fm, the hydrodynamic switching times in the respective simulations. One may wonder whether matching the hydronization times would change any conclusions. Since the flow in the 3 + 1D case is lower, this is not the case. Running the 2 + 1D case up to $\tau = 0.6$ fm only accentuates the difference.

VIII. QUESTION OF THE 2 + 1D LIMIT

In 2 + 1 dimensions, the initial transverse fields E^i and $F_{i\eta}$ are both zero. This originates from the facts that $A_{0,\eta} = 0$ and that nothing depends on η. In 3 + 1 dimensions, the η dependence of E_0^i is dictated by the Gauss law $[D_i, E_0^i] = -[D_\eta, E_0^\eta]$ and the fact that the transverse chromomagnetic field component $F_{i\eta}$ depends on η through $A_{0,\eta}$ and $A_{0,i}$. Ultimately, the η dependence of any term in these expressions comes from the η dependence of V in Eq. (18).

The main issue for the approach to the 2 + 1D initial condition, equivalently the $\sqrt{s} \to \infty$ limit, is how the transverse part of the energy density [τ times $\epsilon_{x,y}$ in Eq. (25)] behaves in that limit. The behavior of the transverse energy density depends on three main components. The first one is how fast the η dependence of V goes away as $\sqrt{s} \to \infty$. The second one is how the initial time τ_0 depends on $\sqrt{s}$. The third one is how fast the field strength grows as $\sqrt{s}$ grows.

The $\sqrt{s}$ dependence of V is in the running coupling constant. From Eq. (19), one can see that $\zeta \propto \sqrt{\alpha_s}$ and hence the Y derivative of V will behave like some power of α_s. As $\sqrt{s} \to \infty$, the running coupling $\alpha_s \to 0$. In this sense, one could argue that the transverse electric field E^i and the magnetic field $F_{i\eta}$ as well as A_η will vanish in the infinite momentum limit, restoring the 2 + 1D initial conditions. This argument, however, is too simple. One needs to take into account the behavior of the gauge field strength and the behavior of τ_0 as well.

Consider the transverse magnetic field

$$F_{i\eta} = \partial_i A_\eta - \partial_\eta A_i - ig[A_i, A_\eta]. \tag{37}$$

Because of the form of the initial gauge fields given in Eqs. (6) and (12), all three terms above contain an η derivative. The transverse electric field E_0^i also depends on the size of η derivatives through the Gauss condition. As argued above, the size of the η derivative is given by some positive power of the strong coupling $\alpha_s(Q_s)$ where $Q_s \sim s^{\lambda/2}$ is the saturation scale. The transverse gauge field components $A_{0,i}$ behave like Q_s/g and ∂_i behaves like Q_s. The initial time τ_0 should behave like $1/Q_s$ or some power of $1/\sqrt{s}$. Putting these all together, one can then argue that at the initial time τ_0

$$\tau_0 \epsilon_i \sim (F_{i\eta})^2/\tau_0 \sim Q_s^a \alpha_s^b \tag{38}$$

where a and b are some positive powers. Since the saturation scale behaves like a power of $\sqrt{s}$, and the coupling constant behaves like an inverse logarithm of $\sqrt{s}$, [$\alpha_s \approx 1/\ln(Q_s)$], the transverse energy density ϵ_i in Eq. (25) cannot vanish as $\sqrt{s} \to \infty$. It will actually diverge. Hence, our 3 + 1D initial conditions, although they inherit many features from the 2 + 1D case, will not recover the 2 + 1D initial conditions in the infinite momentum limit.

Ultimately, whether or not the boost-invariant initial conditions are recovered as $\sqrt{s} \to \infty$ depends on how the η derivatives of the initial fields behave in that limit. The 2 + 1D limit will be recovered only if the η derivatives vanish faster than some negative power of $\sqrt{s}$. There are indeed other 3 + 1D glasma models that do recover the 2 + 1D limit [43,53]. They can do so because their initial conditions do not include as strong longitudinal fluctuations as those provided by the JIMWLK evolution. Consequently, the η derivatives in these models go to zero much faster than α_s does.

A related question is whether we should see in our simulations the Weibel instability observed in various 3 + 1D CYM simulations [36–42]. In Ref. [37], it was shown that the instability-driven exponential growth starts around

$\tau \approx 30/(g^2\mu)$. Taking $1/(g^2\mu) \approx 1/Q_s = O(0.1)$ fm relevant for RHIC and the LHC collisions [36], the exponential growth would start around $\tau = O(1)$ fm. This is similar to or longer than the evolution time of the glasma in our simulations. According to this estimate, the effect of such instability would be weak in our simulations. One should, however, note that the spectrum of the η-dependent fluctuations is quite different in those simulations compared to ours. Investigation of the eventual appearance of the Weibel instability in our setting would be an interesting future study.

IX. HYDRODYNAMIC EVOLUTION AND HADRONIC CASCADE

After the CYM evolution, the stress energy tensor is constructed from the chromoelectric and chromomagnetic fields. The stress energy tensor is diagonalized to yield the local energy density, ϵ, and flow velocity, u^μ, via the Landau condition:

$$T^\mu_\nu u^\nu = \epsilon u^\mu. \tag{39}$$

In previous studies, it was common to initialize hydrodynamics simulations with the ideal stress energy tensor:

$$T^{\mu\nu}_{\text{ideal}} = (\epsilon + P)u^\mu u^\nu - P g^{\mu\nu}. \tag{40}$$

In this paper, the entire stress energy tensor that is generated by 3 + 1D IP-GLASMA is used to initialize 3 + 1D hydrodynamics, and thus no information is lost in the matching condition.

The hydrodynamic stress energy tensor can be decomposed into an ideal part and a viscous part:

$$T^{\mu\nu}_{\text{hydro}} = T^{\mu\nu}_{\text{ideal}} + \pi^{\mu\nu} - \Pi(g^{\mu\nu} - u^\mu u^\nu) \tag{41}$$

where $\pi^{\mu\nu}$ is the shear-stress tensor and Π is the bulk pressure. Since the CYM is conformal, there is no bulk pressure, and the shear stress tensor is simply the difference between the IP-GLASMA energy-momentum tensor and that of ideal hydrodynamics:

$$\pi^{\mu\nu} = T^{\mu\nu} - T^{\mu\nu}_{\text{ideal}}. \tag{42}$$

There is, however, a discontinuity in the relationship between the energy and pressure, i.e., the equation of state (EoS), in the IP-GLASMA phase for which $\epsilon = 3P$ and the hydrodynamic phase for which the EoS comes from lattice QCD calculations [66] matched to a hadronic resonance gas model. This discontinuity in pressure gives the initial bulk pressure:

$$\Pi = \mathrm{P}_{\text{CYM}} - \mathrm{P}_{\text{hotQCD}}(\epsilon) = \epsilon/3 - \mathrm{P}_{\text{hotQCD}}(\epsilon). \tag{43}$$

In this paper, the switching time between the CYM dynamics and hydrodynamics is set to $\tau_h = 0.6$ fm. This switching time is a little later than the one used in the 2 + 1D case (0.4 fm) [28] to allow development of a bit more preflow. The effects of changing τ_h are, however, not extensively studied in the 3 + 1D setting so far and will be left for future studies. The values of the transport coefficients we used are the same as those we used in Ref. [28] except the value of the shear viscosity which is set to $\eta/s = 0.08$ due to the fact that hydrodynamic flow develops slower in the 3 + 1D expansion than in the 2 + 1D expansion as explained in the next section. Switch to URQMD occurs via the Cooper-Frye formula at the hypersurface defined by the switching temperature of 145 MeV.

Altogether, 1200 3 + 1D IP-GLASMA+ MUSIC events were generated in the 0–50% centrality range, or 240 per 10% in each 10% centrality bin. Each one of these events was then sampled for 100 URQMD runs.

X. RESULTS

A. Initial state quantities

Before describing the 3 + 1D results, it is important for us to check whether the additional physics present in the initialization of the fields leads to any differences in the midrapidity physics. For this purpose we show the initial state anisotropy (also known as eccentricity) as characterized by

$$\varepsilon_n = \frac{\int d^2x_\perp r^n e^{in\phi}\epsilon(\mathbf{x}_\perp)}{\int d^2x_\perp r^n \epsilon(\mathbf{x}_\perp)}. \tag{44}$$

Here $\epsilon(\mathbf{x}_\perp)$ is the energy density at $\mathbf{x}_\perp$, $r = |\mathbf{x}_\perp|$, and $\phi = \tan^{-1}(y/x)$. Figure 8(a) compares the eccentricities between the 3 + 1D and 2 + 1D simulations, where the 2 + 1D simulations are from Ref. [28]. The two simulations show the same trends but the ε_n values are systematically larger in the 2 + 1D simulation, particularly at larger centralities. This could be partially due to the smaller number of events for the 3 + 1D case. The 3 + 1D events have an order of magnitude fewer events than the 2 + 1D. As such, it is possible that the tail of the 3 + 1D multiplicity distribution was not fully populated. Figure 8(d) compares the number of binary collisions, N_{bin}, as a function of centrality, as a way of showing how nucleus-nucleus overlap corresponds to centrality. This figure shows that the 2 + 1D curve is slightly steeper as a function of centrality, which is consistent with the more rapid rise in ε_n as a function of centrality shown in Fig. 8(a). The centrality selection done here follows the same procedure discussed in Ref. [28].

In Figs. 8(b) and 8(c), the flow vector components $u^\tau = \gamma$ and the rms values of the spatial components defined as

$$u^\mu_{\text{rms}} = \sqrt{\left\langle \frac{\int d^2x_\perp \epsilon(\mathbf{x}_\perp)(u^\mu)^2}{\int d^2x_\perp \epsilon(\mathbf{x}_\perp)} \right\rangle} \tag{45}$$

are shown. The angular bracket here means the average over the events. These values are measured at the hydrodynamic switching time $\tau = 0.6$ fm for the 3 + 1D simulations and $\tau = 0.4$ fm for the 2 + 1D simulations. Although the 3 + 1D CYM simulations were allowed to run longer, the flow components are still smaller than the 2 + 1D case. This ultimately results from the difference in the behaviors of the pressure component which was discussed in depth in Sec. VII. One consequence of less-developed preflow is that the value of shear viscosity over entropy density, η/s, in 3 + 1D simulations needs to be less than that in 2 + 1D simulations to match the experimental data.

B. Midrapidity observables

While the hydrodynamic evolution allows for some tuning of parameters, such as the transport coefficients, the 3 + 1D IP-GLASMA initialization is able to describe the

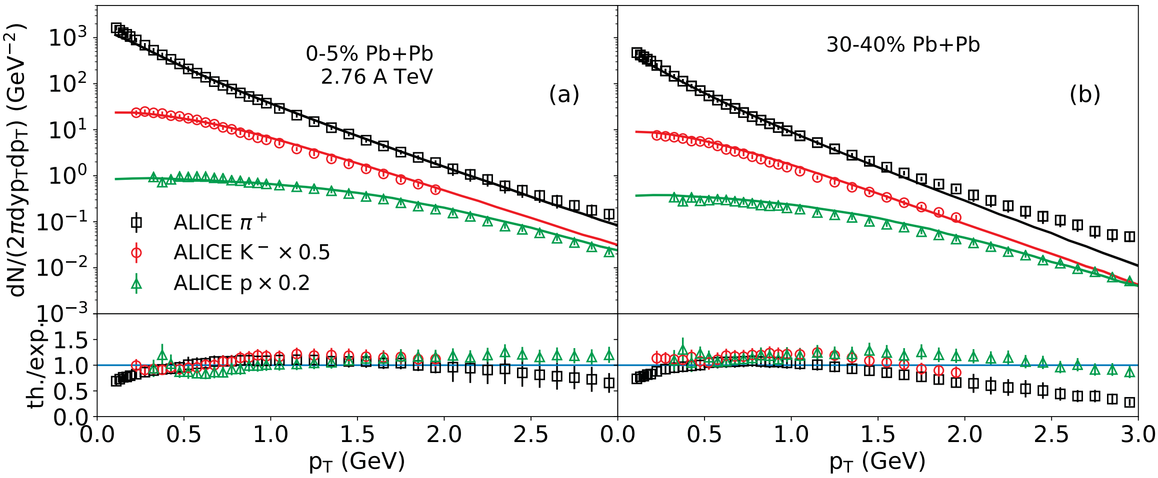

FIG. 9. Identified particle spectrum for two centralities, compared to ALICE data [69]. The lower panels show the ratio of the theoretical data to the experimental calculation for each curve.

essential midrapidity observables. Here, $\eta/s = 0.08$, which differs from the value favored by $2+1$D IP-GLASMA. For example, Ref. [67] which is a recent $2+1$D IP-GLASMA paper and uses the same EOS as this paper has $\eta/s = 0.12$. Our previous calculations using $2+1$D IP-GLASMA [28] used $\eta/s = 0.095$. The difference in η/s is due in part to the differences in preequilibrium flow between the $2+1$D and $3+1$D simulations. The bulk viscosity, $\zeta/s(T)$, is taken from Ref. [68] and is consistent with that typically used in $2+1$D IP-GLASMA simulations, and finds similar agreement with data.

The hadronic spectra are well described, shown for two centrality classes in Fig. 9, as are the particles identified as $\langle p_T\rangle$ in Fig. 10. The differential v_n shown in Fig. 11 have similar behavior to other hydrodynamic calculations that include bulk viscosity: a slight underestimate of the $v_n(p_T)$ at small p_T, say up to $p_T \approx 0.7$ GeV, and a slight overestimate above. Hydrodynamic calculations without bulk viscosity are typically able to describe the $v_n(p_T)$ over a much wider range in p_T but typically overestimate the $\langle p_T\rangle$, particularly for heavier particles such as protons. By including bulk viscosity, one typically improves the spectra and $\langle p_T\rangle$, but degrades agreement with $v_n(p_T)$. It is still possible to find good agreement with the integrated v_n, by missing the $v_n(p_T)$ at small p_T and missing in the opposite direction at high p_T. In this paper, the specific shear viscosity η/s is tuned to find agreement with the integrated v_2.

To summarize, phenomenologically, including bulk viscosity leads to the tradeoff of $v_n(p_T)$ for $\langle p_T\rangle$ and the particle spectra. This can be justified by the fact that the spectra and $\langle p_T\rangle$ are more basic quantities and that $v_n(p_T)$ is sensitive to δf corrections that have large uncertainties, particularly in the case of bulk viscosity.

C. Rapidity dependent observables

The primary purpose of developing a three-dimensional extension of the boost-invariant IP-GLASMA is to explore the longitudinal dynamics of HICs, and we do so in this section.

The initial state events are run in a rapidity window of $[-4, 4]$. In order to avoid sharp gradients at the boundaries in η, it is necessary to put an envelope function on the hydrodynamic evolution that provides a smooth gradient to zero density for $|\eta| > 2.75$. Here, a half Gaussian takes the components of $T^{\mu\nu}$ to zero as follows:

$$T^{\mu\nu}_{\mathrm{hydro}}(\mathbf{x}_\perp, \eta, \tau_h) = T^{\mu\nu}_{\text{IP-GLASMA}}(\mathbf{x}_\perp, \eta, \tau_h) \times \exp\left[-\theta(|\eta| - 2.75|)\frac{(|\eta| - 2.75)^2}{2}\right]. \tag{46}$$

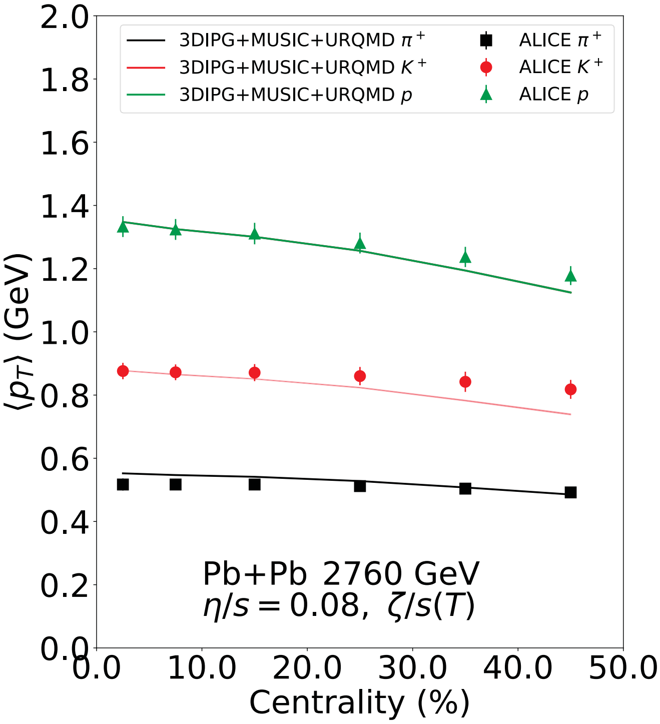

FIG. 10. The particle identified $\langle p_T\rangle$ for Pb-Pb at 2.76 TeV in the 0–5% centrality bin as compared to ALICE data [69].

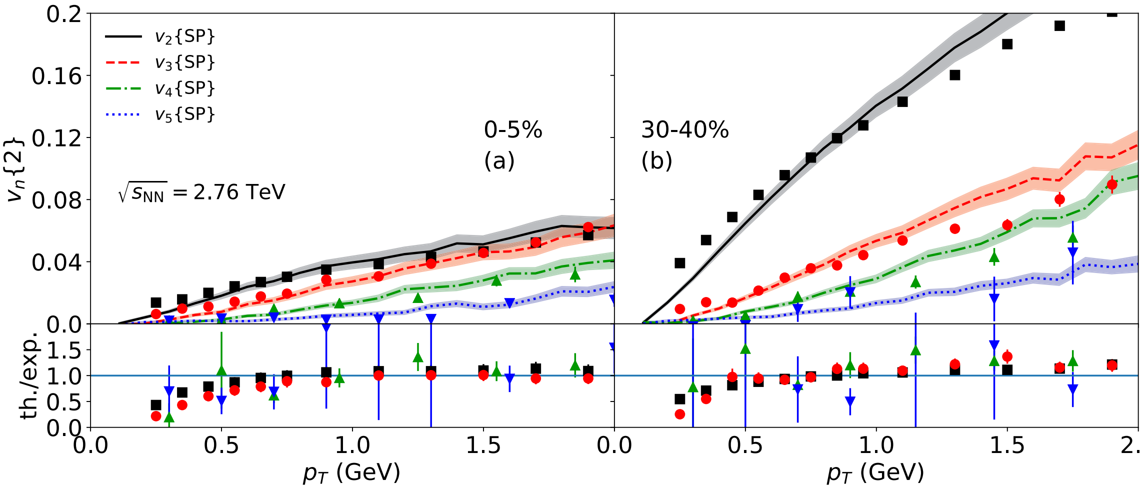

FIG. 11. Differential flow harmonics $v_n\{2\}(p_T)$ for two centralities, compared to ALICE data [70]. Left upper panel: 0–5% centrality. Right upper panel: 30–40% centrality. Lower panels show the ratio of theoretical data to experimental data from the upper panels.

With this envelope, the model can match the pseudorapidity dependence of the charged hadron multiplicity per unit pseudorapidity, $dN_{\rm ch}/d\eta_s$, as plotted in Fig. 12.

The multiplicity distribution $dN_{\rm ch}/d\eta_s$ does not really require sophisticated IP-GLASMA initial states to describe [23] as it is not very sensitive to longitudinal fluctuations. To see the effect of longitudinal fluctuations better, correlation observables are needed. In Figs. 13 and 14, we show our calculations of the flow harmonics as a function of the pseudorapidity following the procedures in Ref. [72] (by ALICE) and Ref. [73] (by CMS). The main differences between the ALICE and the CMS measurements are the reference ranges ($|\eta| < 0.5$ for ALICE and $|\eta| < 2.4$ for CMS) and the p_T ranges ($p_T > 0$ for ALICE and $0.3 < p_T < 3.0$ GeV for CMS).

In Fig. 14, $v_2(\eta)$ is compared to CMS data, using their kinematic cuts of p_T and η. The flow harmonic $v_2(\eta)$ has a very mild rapidity dependence and the calculation shows similar behavior. The CMS data use reference particles over a range η that is a much wider range than that used by ALICE in Fig. 13. This likely contributes to the steeper rapidity dependence in the ALICE data, because one would expect a more peaked structure at midrapidity when correlating with midrapidity, as seen in the data. It is, however, apparent that the current 3 + 1D IP-GLASMA initial conditions do not contain enough longitudinal decorrelations to describe the ALICE data. This may be remedied by introducing thermal fluctuations in the hydrodynamic evolution. It is also possible that the fact that our calculations underestimate $v_n(p_T)$ in the low momentum region may also contribute to the discrepancy, but this needs to be investigated further.

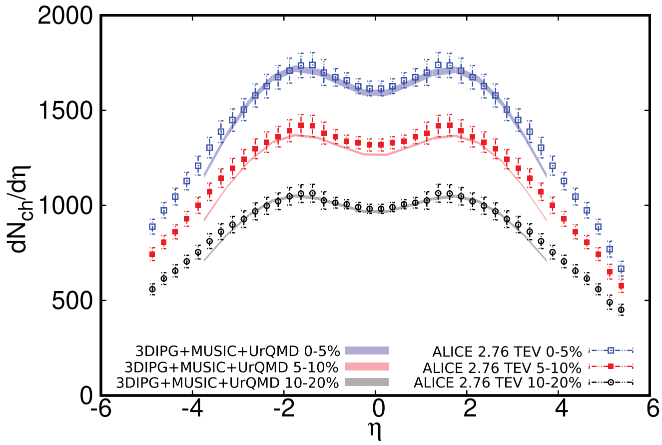

FIG. 12. Charged hadron multiplicity as a function of rapidity, as compared to ALICE data [71].

We have also calculated the rapidity correlation $r_n(\eta_a, \eta_b)$ [74]. However, as the number of events we have so far (240 3 + 1D IP-GLASMA+MUSIC events per 10% centrality) turned out to be too small to make statistically meaningful statements, we will leave it for future study.

XI. CONCLUSION

The purpose of this paper is to introduce a realistic model of 3 + 1D initial conditions for relativistic heavy ion collision simulations. The IP-GLASMA model, originally developed for 2 + 1D simulations, has had great phenomenological success for description of the midrapidity observables that reflect the underlying QGP dynamics. To extend the reach of theoretical descriptive and predictive power to 3 + 1 dimensions, it is imperative to develop a realistic extension of the IP-GLASMA initial conditions. Furthermore, hydrodynamic and hadronic cascade simulations of heavy ion collisions are capable of handling 3 + 1D dynamics. As these simulations are sensitive to the initial conditions, it is crucial to develop realistic 3 + 1D initial conditions.

Owing to the fact that the simplicity of the 2 + 1D formulation comes from the assumption of the infinite momentum frame (equivalently, boost invariance), the extension is not just a matter of trivially adding one more dimension to the 2 + 1D IP-GLASMA. In this paper, we have made an effort to preserve the simplicity of the 2 + 1D formulation as much as possible while breaking the boost invariance.

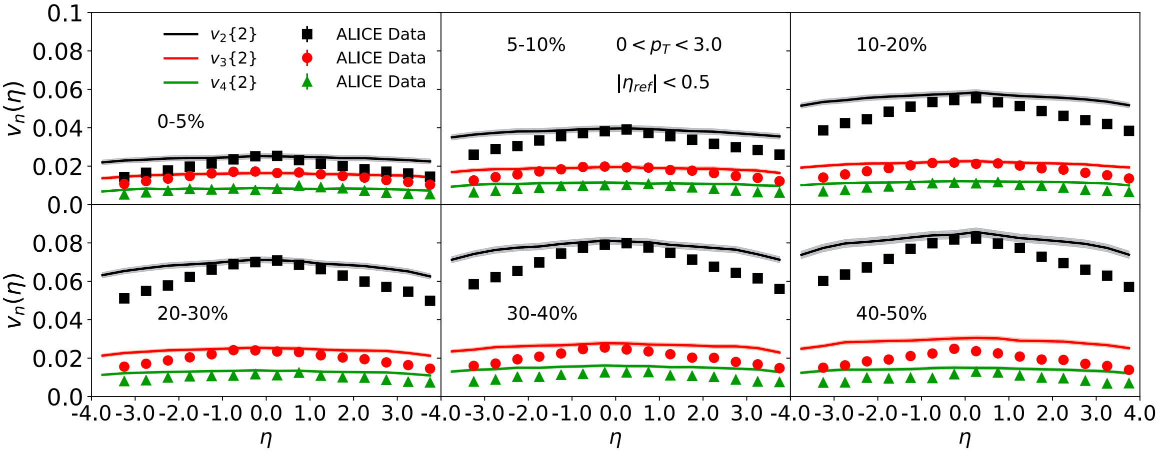

FIG. 13. The rapidity dependence of the momentum anisotropies $v_n(\eta)(n = 2, 3, 4)$, compared to ALICE data [72]. Both data and the calculation are for $p_T > 0$ GeV and use reference particles at midrapidity ($|\eta| \leqslant 0.5$).

Our way of doing so is to generate longitudinal structure in the precollision gluon fields through the JIMWLK evolution, the numerical implementation of which was developed in Ref. [35]. This was incorporated in the IP-GLASMA model in Ref. [52]. There remain theoretical difficulties in temporally evolving this system on the lattice in three spatial dimensions, however. These include the difficulty posed by the initial gauge fields and the initial solution to Gauss's law, as outlined in Sec. IV. Both of these problems are addressed in this paper, although the solutions may not be unique. This allows for a temporal evolution in three spatial dimensions and thus exploration of the phenomenological effects of the longitudinal structure generated by the JIMWLK equations. The $3 + 1$D IP-GLASMA simulation is coupled to MUSIC and URQMD for comparison to hadronic results.

The $2 + 1$D IP-GLASMA describes the transverse dynamics of heavy ion collisions extremely well. With slightly modified parameters, the $3 + 1$D implementation is able to achieve a similar level of agreement to key observables such as $\langle p_T \rangle$, particle spectra, and p_T-integrated v_n. In addition, the $3 + 1$D IP-GLASMA is able to explore longitudinal observables. In this paper, the multiplicity and v_n flow harmonics are explored as a function of pseudorapidity, and good agreement is found. Comparison to higher order correlations involving the longitudinal direction will be explored in a future work, once substantially better statistics are generated. This paper serves as a proof of principle that the IP-GLASMA can be generalized to $3 + 1$D in a way that allows for consistent temporal evolution on the lattice and thus phenomenological application.

ACKNOWLEDGMENTS

We acknowledge the support of the Natural Sciences and Engineering Research Council of Canada (Grants No. SAPIN-2018-00024 and No. SAPIN-2020-00048). Computations were made on the Beluga supercomputer system from McGill University, managed by Calcul Québec and Digital Research Alliance of Canada. The operation of this supercomputer is funded by the Canada Foundation for Innovation, Ministère de l'Économie, des Sciences et de l'Innovation du Québec and le Fonds de Recherche du Québec—Nature et Technologies. We also gratefully acknowledge R. Fries, S.

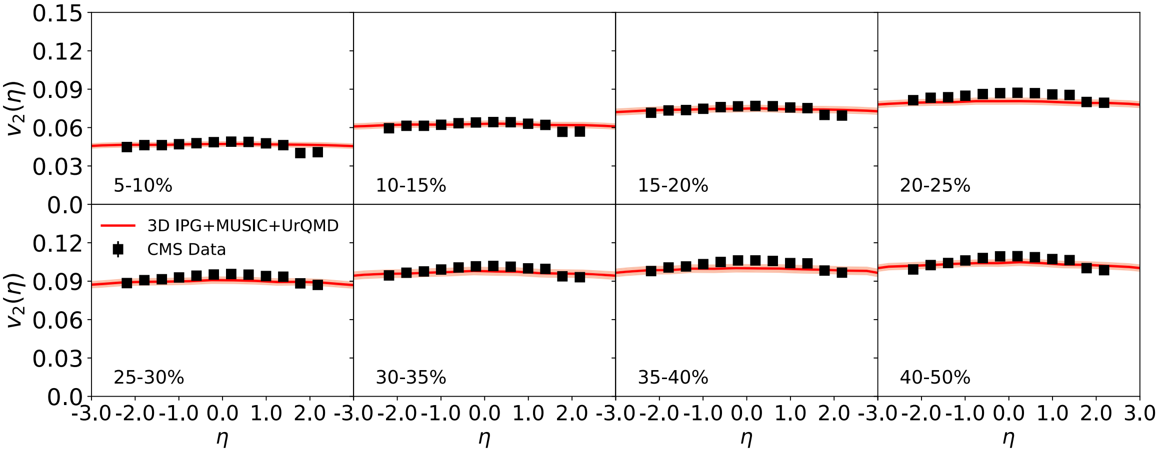

FIG. 14. The rapidity dependence of $v_2(\eta)$, compared to CMS data [73]. Both the CMS data and the calculation are for $0.3 < p_T < 3.0$ GeV and references particles in $|\eta| \leqslant 2.4$.

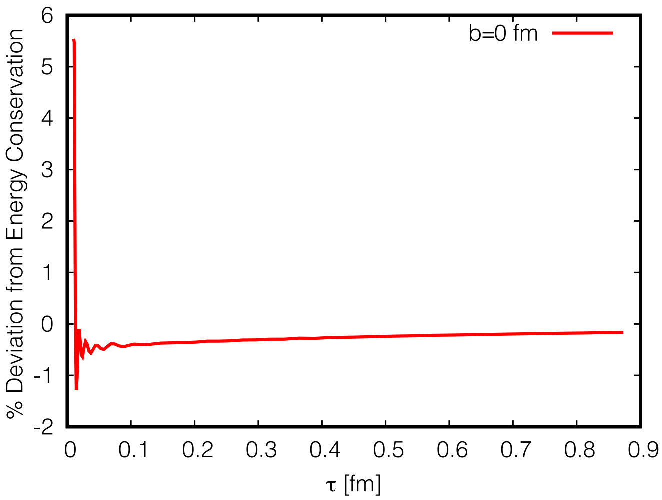

FIG. 15. Temporal evolution of (B5). Despite fluctuations at very early times, energy is nicely conserved throughout the evolution of the system. This figure is a typical event with $b = 0$ fm.

Hauksson, A. Ipp, L. Leuthner, D. I. Müller, B. Schenke, S. Schlichting, and R. Venugopalan for insightful discussions.

APPENDIX A: SOLUTION TO GAUSS's LAW

As mentioned, using the ansatz in Eq. (16) turns Gauss's law Eq. (11) into the covariant Poisson equation. We use a modified Jacobi method for solving the Poisson equation to find the initial transverse E fields that satisfy Gauss's law:

$$\nabla^2_\perp \phi = -\rho.$$

Discretizing, and solving for $\phi_{i,j}$,

$$\frac{\phi_{i+1,j} + \phi_{i-1,j} - 2\phi_{i,j}}{h^2} + \frac{\phi_{i,j+1} + \phi_{i,j-1} - 2\phi_{i,j}}{h^2} = -\rho_{i,j}, \tag{A1}$$

$$\phi_{i,j} = \frac{1}{4}(\phi_{i+1,j} + \phi_{i-1,j} + \phi_{i,j+1} + \phi_{i,j-1} + h^2\rho_{i,j}). \tag{A2}$$

Then the iterative procedure is given by

$$\phi^{n+1}_{i,j} = \tfrac{1}{4}\big(\phi^n_{i+1,j} + \phi^n_{i-1,j} + \phi^n_{i,j+1} + \phi^n_{i,j-1} + h^2\rho^n_{i,j}\big). \tag{A3}$$

For covariant derivatives, all quantities should be parallel transported:

$$\phi^{n+1}_{i,j} = \tfrac{1}{4}\big(U_{i,j}\phi^n_{i+1,j}U^\dagger_{i,j} + U^\dagger_{i-1,j}\phi^n_{i-1,j}U_{i-1,j} + \tag{A4}$$

$$U_{i,j}\phi^n_{i,j+1}U^\dagger_{i,j} + U^\dagger_{i,j-1}\phi^n_{i,j-1}U_{i,j-1} + h^2\rho^n_{i,j}\big). \tag{A5}$$

APPENDIX B: CONSERVATION OF ENERGY

The statement of energy conservation in Milne coordinates is

$$\partial_\tau T^{\tau\tau} + \partial_\perp T^{\perp\tau} + \partial_\eta T^{\eta\tau} = -\tau T^{\eta\eta} - T^{\tau\tau}/\tau. \tag{B1}$$

Multiplying by τ and collecting terms gives

$$\partial_\tau(\tau T^{\tau\tau}) + \partial_\perp(\tau T^{\perp\tau}) + \partial_\eta(\tau T^{\eta\tau}) = -\tau^2 T^{\eta\eta}. \tag{B2}$$

Integrating over the four-dimensional volume $(dxdyd\eta d\tau)$,

$$\big(\Delta T^{\tau\tau}_{\text{total}}\big) + \int dxdyd\eta d\tau\, \partial_\eta(\tau T^{\eta\tau}) = -\int dxdyd\eta d\tau(\tau^2 T^{\eta\eta}). \tag{B3}$$

The second term becomes a boundary term:

$$\big(\Delta T^{\tau\tau}_{\text{total}}\big) + \left(\int dxdyd\tau(\tau T^{\eta\tau})\right)\Bigg|^{\eta_{max}}_{\eta_{min}} = -\int dxdyd\eta d\tau(\tau^2 T^{\eta\eta}). \tag{B4}$$

In Fig. 15, the deviation of the ratio of the left-hand side to the right-hand side of Eq. (B4) from unity is plotted. Explicitly, the quantity on the y axis is

$$\left(1 - \frac{\int dxdyd\eta(\tau T^{\tau\tau})\Big|^{\tau_{max}}_{\tau_{min}} + \big(\int dxdyd\tau(\tau T^{\eta\tau})\big)\Big|^{\eta_{max}}_{\eta_{min}}}{-\int dxdyd\eta d\tau(\tau^2 T^{\eta\eta})}\right) \times 100\%. \tag{B5}$$

There is deviation from energy conservation at extremely early times, likely due to lattice effects, but the ratio approaches and remains close to zero for the rest of the evolution. This indicates that energy is conserved to within about 1% throughout most of the simulation.

---

[1] J. Adams *et al.* (STAR Collaboration), Nucl. Phys. A **757**, 102 (2005).
[2] K. Adcox *et al.* (PHENIX Collaboration), Nucl. Phys. A **757**, 184 (2005).
[3] M. Arslandok *et al.*, arXiv:2303.17254.
[4] S. A. Bass *et al.*, Prog. Part. Nucl. Phys. **41**, 255 (1998).
[5] H. Petersen, D. Oliinychenko, M. Mayer, J. Staudenmaier, and S. Ryu, Nucl. Phys. A **982**, 399 (2019).
[6] J. Sollfrank, P. Huovinen, M. Kataja, P. V. Ruuskanen, M. Prakash, and R. Venugopalan, Phys. Rev. C **55**, 392 (1997).
[7] P. Huovinen, P. V. Ruuskanen, and J. Sollfrank, Nucl. Phys. A **650**, 227 (1999).
[8] P. F. Kolb, P. Huovinen, U. W. Heinz, and H. Heiselberg, Phys. Lett. B **500**, 232 (2001).
[9] M. Gyulassy, I. Vitev, X.-N. Wang, and P. Huovinen, Phys. Lett. B **526**, 301 (2002).
[10] U. W. Heinz, H. Song, and A. K. Chaudhuri, Phys. Rev. C **73**, 034904 (2006).
[11] P. Huovinen and P. V. Ruuskanen, Annu. Rev. Nucl. Part. Sci. **56**, 163 (2006).
[12] R. Baier, P. Romatschke, and U. A. Wiedemann, Phys. Rev. C **73**, 064903 (2006).
[13] H. Song and U. W. Heinz, Phys. Rev. C **77**, 064901 (2008).

[14] C. Shen, U. Heinz, P. Huovinen, and H. Song, Phys. Rev. C **82**, 054904 (2010).

[15] C. Shen, U. Heinz, P. Huovinen, and H. Song, Phys. Rev. C **84**, 044903 (2011).

[16] Z. Qiu, C. Shen, and U. Heinz, Phys. Lett. B **707**, 151 (2012).

[17] C. Gale, S. Jeon, and B. Schenke, Int. J. Mod. Phys. A **28**, 1340011 (2013).

[18] S. Jeon and U. Heinz, Int. J. Mod. Phys. E **24**, 1530010 (2015).

[19] D. H. Rischke, S. Bernard, and J. A. Maruhn, Nucl. Phys. A **595**, 346 (1995).

[20] C. Nonaka, E. Honda, and S. Muroya, Eur. Phys. J. C **17**, 663 (2000).

[21] T. Hirano, K. Morita, S. Muroya, and C. Nonaka, Phys. Rev. C **65**, 061902(R) (2002).

[22] B. Schenke, S. Jeon, and C. Gale, Phys. Rev. Lett. **106**, 042301 (2011).

[23] B. Schenke, S. Jeon, and C. Gale, Phys. Rev. C **82**, 014903 (2010).

[24] B. Schenke, P. Tribedy, and R. Venugopalan, Phys. Rev. C **86**, 034908 (2012).

[25] B. Schenke, P. Tribedy, and R. Venugopalan, Phys. Rev. Lett. **108**, 252301 (2012).

[26] H. Kowalski and D. Teaney, Phys. Rev. D **68**, 114005 (2003).

[27] C. Gale, S. Jeon, B. Schenke, P. Tribedy, and R. Venugopalan, Phys. Rev. Lett. **110**, 012302 (2013).

[28] S. McDonald, C. Shen, F. Fillion-Gourdeau, S. Jeon, and C. Gale, Phys. Rev. C **95**, 064913 (2017).

[29] A. Ayala, J. Jalilian-Marian, L. D. McLerran, and R. Venugopalan, Phys. Rev. D **53**, 458 (1996).

[30] J. Jalilian-Marian, A. Kovner, L. D. McLerran, and H. Weigert, Phys. Rev. D **55**, 5414 (1997).

[31] E. Iancu, A. Leonidov, and L. D. McLerran, Phys. Lett. B **510**, 133 (2001).

[32] J.-P. Blaizot, E. Iancu, and H. Weigert, Nucl. Phys. A **713**, 441 (2003).

[33] F. Gelis, T. Lappi, and R. Venugopalan, Phys. Rev. D **78**, 054019 (2008).

[34] F. Gelis, T. Lappi, and R. Venugopalan, Phys. Rev. D **78**, 054020 (2008).

[35] T. Lappi and H. Mäntysaari, Eur. Phys. J. C **73**, 2307 (2013).

[36] P. Romatschke and R. Venugopalan, Phys. Rev. Lett. **96**, 062302 (2006).

[37] P. Romatschke and R. Venugopalan, Phys. Rev. D **74**, 045011 (2006).

[38] K. Fukushima, F. Gelis, and L. McLerran, Nucl. Phys. A **786**, 107 (2007).

[39] K. Fukushima and F. Gelis, Nucl. Phys. A **874**, 108 (2012).

[40] J. Berges and S. Schlichting, Phys. Rev. D **87**, 014026 (2013).

[41] K. Dusling, T. Epelbaum, F. Gelis, and R. Venugopalan, Phys. Rev. D **86**, 085040 (2012).

[42] T. Epelbaum and F. Gelis, Phys. Rev. D **88**, 085015 (2013).

[43] D. Gelfand, A. Ipp, and D. Müller, Phys. Rev. D **94**, 014020 (2016).

[44] T. Lappi, Eur. Phys. J. C **55**, 285 (2008).

[45] L. D. McLerran and R. Venugopalan, Phys. Rev. D **49**, 2233 (1994).

[46] L. D. McLerran and R. Venugopalan, Phys. Rev. D **49**, 3352 (1994).

[47] A. Kovner, L. D. McLerran, and H. Weigert, Phys. Rev. D **52**, 3809 (1995).

[48] A. Kovner, L. D. McLerran, and H. Weigert, Phys. Rev. D **52**, 6231 (1995).

[49] C. S. Lam and G. Mahlon, Phys. Rev. D **62**, 114023 (2000).

[50] Ş. Özönder and R. J. Fries, Phys. Rev. C **89**, 034902 (2014).

[51] L. D. McLerran and R. Venugopalan, Phys. Lett. B **424**, 15 (1998).

[52] B. Schenke and S. Schlichting, Phys. Rev. C **94**, 044907 (2016).

[53] S. Schlichting and P. Singh, Phys. Rev. D **103**, 014003 (2021).

[54] A. Ipp, D. I. Müller, S. Schlichting, and P. Singh, Phys. Rev. D **104**, 114040 (2021).

[55] B. Schenke, S. Schlichting, and P. Singh, Phys. Rev. D **105**, 094023 (2022).

[56] A. Ipp, M. Leuthner, D. I. Müller, S. Schlichting, and P. Singh, EPJ Web Conf. **274**, 05017 (2022).

[57] K. Werner, I. Karpenko, T. Pierog, M. Bleicher, and K. Mikhailov, Phys. Rev. C **82**, 044904 (2010).

[58] C. Shen and B. Schenke, Phys. Rev. C **97**, 024907 (2018).

[59] T. Epelbaum and F. Gelis, Nucl. Phys. A **926**, 122 (2014).

[60] S. Schlichting and B. Schenke, Phys. Lett. B **739**, 313 (2014).

[61] K. Rummukainen and H. Weigert, Nucl. Phys. A **739**, 183 (2004).

[62] A. Kurkela, A. Mazeliauskas, J.-F. Paquet, S. Schlichting, and D. Teaney, Phys. Rev. C **99**, 034910 (2019).

[63] C. Gale, J.-F. Paquet, B. Schenke, and C. Shen, Phys. Rev. C **105**, 014909 (2022).

[64] W. Florkowski and R. Ryblewski, Phys. Rev. C **83**, 034907 (2011).

[65] W. Florkowski, R. Ryblewski, and M. Strickland, Phys. Rev. C **88**, 024903 (2013).

[66] A. Bazavov *et al.* (HotQCD Collaboration), Phys. Rev. D **90**, 094503 (2014).

[67] B. Schenke, C. Shen, and P. Tribedy, Phys. Rev. C **102**, 044905 (2020).

[68] S. Ryu, J. F. Paquet, C. Shen, G. S. Denicol, B. Schenke, S. Jeon, and C. Gale, Phys. Rev. Lett. **115**, 132301 (2015).

[69] B. Abelev *et al.* (ALICE Collaboration), Phys. Rev. C **88**, 044910 (2013).

[70] K. Aamodt *et al.* (ALICE Collaboration), Phys. Rev. Lett. **107**, 032301 (2011).

[71] E. Abbas *et al.* (ALICE Collaboration), Phys. Lett. B **726**, 610 (2013).

[72] J. Adam *et al.* (ALICE Collaboration), Phys. Lett. B **762**, 376 (2016).

[73] S. Chatrchyan *et al.* (CMS Collaboration), Phys. Rev. C **87**, 014902 (2013).

[74] S. McDonald, S. Jeon, and C. Gale, Nucl. Phys. A **1005**, 121771 (2021).